The Astronomical Journal, 150:54 (12pp), 2015 August doi:10.1088/0004-6256/150/2/54

RADAR IMAGING AND CHARACTERIZATION OF THE BINARY NEAR-EARTH ASTEROID (185851) 2000 DP107

S. P. Naidu[1], J. L. Margot[1,2], P. A. Taylor[3], M. C. Nolan[3], M. W. Busch[4], L. A. M. Benner[5], M. Brozovic[5], J. D. Giorgini[5], J. S. Jao[5], and C. Magri[6]
[1] Department of Earth, Planetary, and Space Sciences, University of California, Los Angeles, 595 Charles Young Drive East, Los Angeles, CA 90095, USA
[2] Department of Physics and Astronomy, University of California, Los Angeles, 430 Portola Plaza, Los Angeles, CA 90095, USA
[3] Arecibo Observatory, HC3 Box 53995, Arecibo, PR 00612, USA
[4] SETI Institute, 189 Bernardo Ave. Suite 100, Mountain View, Mountain View, CA 94043, USA
[5] Jet Propulsion Laboratory, California Institute of Technology, Pasadena, CA 91109-8099, USA
[6] University of Maine at Farmington, 173 High Street, Preble Hall, Farmington, ME 04938, USA
Received 2015 March 5; accepted 2015 June 15; published 2015 July 23

ABSTRACT

The potentially hazardous asteroid (185851) 2000 DP107 was the first binary near-Earth asteroid to be imaged. Radar observations in 2000 provided images at 75 m resolution that revealed the shape, orbit, and spin-up formation mechanism of the binary. The asteroid made a more favorable flyby of the Earth in 2008, yielding images at 30 m resolution. We used these data to obtain shape models for the two components and to improve the estimates of the mutual orbit, component masses, and spin periods. The primary has a sidereal spin period of 2.7745 ± 0.0007 hr and is roughly spheroidal with an equivalent diameter of 863 m ± 5%. It has a mass of 4.656 ± 0.43 × 10^{11} kg and a density of 1381 ± 244 kg m^{-3}. It exhibits an equatorial ridge similar to the (66391) 1999 KW4 primary; however, the equatorial ridge in this case is not as regular and has a ∼300 m diameter concavity on one side. The secondary has a sidereal spin period of 1.77 ± 0.02 days commensurate with the orbital period. The secondary is slightly elongated and has overall dimensions of 377 × 314 × 268 m (6% uncertainties). Its mass is 0.178 ± 0.021 × 10^{11} kg and its density is 1047 ± 230 kg m^{-3}. The mutual orbit has a semimajor axis of 2.659 ± 0.08 km, an eccentricity of 0.019 ± 0.01, and a period of 1.7556 ± 0.0015 days. The normalized total angular momentum of this system exceeds the amount required for the expected spin-up formation mechanism. An increase of angular momentum from non-gravitational forces after binary formation is a possible explanation. The two components have similar radar reflectivity, suggesting a similar composition consistent with formation by spin-up. The secondary appears to exhibit a larger circular polarization ratio than the primary, suggesting a rougher surface or subsurface at radar wavelength scales.

Key words: minor planets, asteroids: individual (2000 DP107) – techniques: radar astronomy

1. INTRODUCTION

Asteroid (185851) 2000 DP107 was discovered on 2000 February 29 by the Lincoln Near-Earth Asteroid Research program in New Mexico. Radar observations in October of that year revealed the asteroid to be a binary system (Margot et al. 2002), the first such system to be imaged in the near-Earth asteroid (NEA) population. The radar data were instrumental in establishing that NEA satellites form by a spin-up and rotational fission process (Margot et al. 2002). Additional radar and photometric studies showed that ∼15% of all NEAs larger than 200 m are binary in nature (Pravec et al. 1999, 2006; Margot et al. 2002). For a recent review of the properties of binary asteroids, see Margot et al. (2015).

The presence of a satellite around the primary gives us an opportunity to secure direct measurements of several quantities that are not normally measurable. Radar observations enable calculations of the orbital period and orbital separation, which reveal the total mass of the binary system through Kepler's third law. In addition, radar observations enable measurements of the masses of individual components by measuring the distances of the component centers of mass (COMs) from the system COM. Using this information, along with the shape models of the two components derived from radar images, we can estimate their densities. These are important constraints for testing models of formation and evolution of NEAs.

Radar observations of 2000 DP107 in 2000 October yielded rough estimates of masses, sizes, and densities of the two components as well as their mutual orbit (Margot et al. 2002). In 2008 September, the asteroid made another close approach to the Earth and was observed at a distance of ∼0.06 astronomical units (au) or about 20 lunar distances. Because this was about half the distance of the 2000 encounter (∼0.11 au), it resulted in data sets with a signal-to-noise ratio (S/N) ∼20 times higher than in 2000. The high S/N enabled us to derive component shapes with effective resolutions of ∼50 m on the surface, and estimate the component masses, volumes, and densities more accurately than was possible in Margot et al. (2002).

In this paper we present detailed component shape models, improved estimates of component masses and densities, and estimates of the mutual orbit parameters using the 2000 and the 2008 radar data. This detailed characterization of 2000 DP107 and its favorable accessibility ($\Delta v \approx 5.9$ km s^{-1}) make it a good candidate for spacecraft rendezvous missions. 2000 DP107 was the target of the PROCYON mission (Funase et al. 2014), which had a planned flyby of the asteroid in 2016. However, the mission suffered an engine failure and will be unable to perform the flyby.

2. METHODS

2.1. Observing and Data Processing

We observed 2000 DP107 using the Arecibo S-band (2380 MHz, 13 cm) radar and the Goldstone X-band (8560 MHz, 3.5 cm) radar on 10 days between 2008 September

9 and 24, during which the asteroid moved ~60° across the sky. It came closest to Earth on September 11 at a distance of 0.057 au. Most of the observing time was dedicated to range-Doppler imaging, with the remainder dedicated to collecting continuous wave (CW) spectra.[7] We obtained 335 range-Doppler images and 65 CW spectra using Arecibo, and 534 range-Doppler images and 67 CW spectra using Goldstone.

Radar observations were performed according to the methods described in Naidu et al. (2013). Briefly, radar imaging was carried out by transmitting a repeating pseudo-random code modulated over a circularly polarized carrier wave, using a binary phase shift keying scheme (Proakis & Salehi 2007). In each *run*, the waveform was transmitted for approximately the round-trip light time (RTT) before switching over to the receiver. The received signal was demodulated and then decoded by cross-correlating it with a replica of the transmitted code, yielding a range resolution equivalent to the baud length of the transmitted code. In each range bin, consecutive returns were fast Fourier transformed (FFT) to obtain the received signal power as a function of Doppler frequency. The end product is a two-dimensional array or image showing the echo power as a function of relative range and Doppler frequency. Note that the observable measured at the telescope is not range, but the round-trip light time to the target. We obtained the relative range between adjacent bins by multiplying the baud length of the code by half the speed of light. We use the term range-Doppler for convenience in this paper, but the word range should not be construed as absolute range.

For CW runs, a monochromatic wave was transmitted for the RTT to the asteroid before switching over to the receiver. The received signal was demodulated, sampled, and recorded. An FFT was applied to the echo timeseries to obtain the CW spectra.

Table 1 summarizes our observations. Because of the smaller antenna size and transmitter power, the Goldstone data have much lower S/N (~1/20) compared to the Arecibo data. Six to eight consecutive Goldstone runs were summed incoherently in order to improve the S/N.

2.2. Mutual Orbit

We used a least-squares procedure similar to that used in both Margot et al. (2002) and Ostro et al. (2006) to fit Keplerian orbits to the positions of the secondary COM with respect to the primary COM. We used data from 2000 October and 2008 September, and initialized the fitting procedure with thousands of distinct initial conditions spanning the entire range of plausible values for all orbital parameters. From the 2000 data, we selected 2–4 images on each day from September 30 to October 7, or 20 measurement epochs spanning 8 days, yielding 20 range separations and 20 Doppler separations. For the 2008 data set, we measured the component COM separations in 10 Arecibo images on each day of Arecibo observations, and in 6, 3, 6, 2, and 8 Goldstone images on September 9, 10, 11, 12, and 13, respectively, giving us a total of 95 measurement epochs spanning 16 days, or 190 measurements (95 range separations and 95 Doppler separations).

We obtained range-Doppler separations between the primary and secondary COMs using two different techniques. In the first approach we estimated the COM locations in the images by measuring the positions of the leading edges (LEs) and trailing edges (TEs) of the components. In the second approach we relied on shape models obtained with `shape` software (Hudson 1993; Magri et al. 2007) to locate the component COMs. If the shape models are accurate, the second technique could yield superior estimates of the COM positions, and therefore of the mutual orbit parameters. Sections 2.3 and 2.4 describe the shape modeling details.

For the first, edge-based approach, we defined the LEs and TEs in the images on the basis of a 3σ signal threshold, where σ is the standard deviation of the background noise. The LE was defined as the first range bin where the object had a signal higher than 3σ, whereas the TE was defined as the last range bin where at least half of the pixels along the Doppler extent exceeded the 3σ threshold. The location of this threshold depends on the Doppler resolution (shown in Table 1). The primary and secondary were assumed to be roughly spherical and their radii were estimated from radar images to be roughly 450 and 150 m, respectively. With these assumptions the range coordinates of the component COMs were taken to be 450 m and 150 m behind their respective LEs. The Doppler coordinates of the COMs were assumed to be located in the middle of the Doppler extent on the TE. Conservative uncertainties of 2–3 times the range and Doppler resolutions were assigned to the range-Doppler separations.

For the second, `shape`-based approach, we used shape modeling software to locate the component COMs under a uniform density assumption. `shape` aligns the synthetic radar images derived from the shape models with the observed radar images, and outputs the COM positions used for the alignment with sub-pixel precision. Uncertainties on the order of the image resolution were assigned to the `shape`-based range and Doppler separations. We computed the COM separations at the same epochs as those used in the edge-based approach.

We fit the mutual orbit and component shapes in an iterative manner. Each iteration started with mutual orbit fitting followed by component shape modeling. In the first iteration, we used the edge-based approach to determine the preliminary mutual orbit and used the orbit solution (orbit pole and longitude of pericenter) to inform our component shape modeling (Sections 2.3 and 2.4). For the second iteration, the best-fit component shapes from the first iteration were used to refine the COM separation estimates using the `shape`-based approach. These improved primary–secondary separation estimates were used to refine the mutual orbit fit. The refined mutual orbit solution was used to obtain the final shape models of the components.

2.3. Primary Shape

We used the `shape` software (Hudson 1993; Magri et al. 2007) to invert the sequence of range-Doppler images and CW spectra from 2008 to obtain a 3D shape model for the primary. Our data set consisted of 278 Arecibo range-Doppler images and 95 CW spectra from both Arecibo and Goldstone, covering a 16 day period between 2008 September 9 and 24. We left out the low-resolution Arecibo images from September 24 and all the Goldstone images as they did not improve the quality of the fit and slowed down the shape modeling process. Because we modeled the primary and secondary separately, we edited the images and spectra to exclude the contribution of the other component to the echoes.

[7] The word continuous is used to distinguish this transmission mode from range modulated operation.

Table 1
Radar Observations of (185851) 2000 DP107 in 2008

Tel	UT Date (yyyy-mmm-dd)	Eph	RTT (s)	P_{tx} (kW)	Baud (μs)	Prim. Res. (Hz)	Sec. Res. (Hz)	Code	Start–stop (hhmmss-hhmmss)	Runs
G	2008 Sep 09	85	59	445	1.0	⋯	⋯	127	114323–114719	3
		87			1.0	⋯	⋯	127	121534–152227	96
					cw	1.0	⋯	none	153128–154316	7
G	2008 Sep 10	89	58	445	cw	1.0	⋯	none	100115–100907	5
					0.5	⋯	⋯	8191	102915–152812	153
					cw	1.0	⋯	none	153412–154908	7
A	2008 Sep 10	89	58	628	cw	0.2	⋯	none	101757–102635	5
				611	0.2	0.08	0.04	65535	102829–114008	37
				561	cw	0.2	⋯	none	114159–115234	6
A	2008 Sep 11	89	58	630	cw	0.2	⋯	none	094357–095235	5
				616	0.2	0.08	0.04	65535	095452–112810	48
				580	cw	0.2	⋯	none	113030–114115	6
G	2008 Sep 12	89	58	430	cw	1.0	⋯	none	095102–100843	10
					0.5	⋯	⋯	8191	101952–142936	128
					cw	1.0	⋯	none	143725–145705	11
A	2008 Sep 13	89	59	603	cw	0.2	⋯	none	084405–085301	5
					0.2	0.08	0.04	65535	085548–105703	57
				570	cw	0.2	⋯	none	105927–110823	5
G	2008 Sep 13	89	59	432	cw	1.0	⋯	none	091304–092304	5
					1.0	⋯	⋯	8191	103240–124441	67
					cw	1.0	⋯	none	125127–131326	12
G	2008 Sep 14	89	60	432	cw	1.0	⋯	none	092211–094047	10
					1.0	⋯	⋯	8191	095318–112614	47
					1.0	⋯	⋯	8191	114209–130244	40
A	2008 Sep 15	89	63	∼604	cw	0.2	⋯	none	075347–080310	5
					0.2	0.08	0.04	65535	080616–102000	56
				585	cw	0.2	⋯	none	102236–102952	4
A	2008 Sep 18	89	70	595	cw	0.2	⋯	none	065646–070944	6
					0.5	0.24	⋯	8191	071531–092200	54
					cw	0.2	⋯	none	092751–093340	3
A	2008 Sep 21	89	81	590	cw	0.2	⋯	none	060205–061410	5
				624	0.5	0.24	⋯	8191	062313–082654	45
A	2008 Sep 24	89	93	660	cw	0.2	⋯	none	052205–053607	5
				680	1.0	⋯	⋯	8191	053910–073632	38
				605	cw	0.2	⋯	none	073910–075312	5

Note. The first column indicates the telescope: Arecibo (A) or Goldstone (G). Eph is the ephemeris solution number used. RTT is the round-trip light time to the target. P_{tx} is the transmitter power. Baud is the delay (i.e., range) resolution (bauds of 0.2, 0.5, and 1 μs correspond to range resolutions of 30, 75, and 150 m, respectively). Prim. res. and Sec. res. are the frequency (i.e., Doppler) resolutions of the processed data for the primary and secondary shape modeling, respectively. Note that the Doppler spread of the target scales linearly with the transmitter frequency. Code is the length of the pseudo-random code used. The timespans of the received data are listed by their UT start and stop times. The last column indicates the number of runs acquired in each configuration.

Shape modeling was generally carried out in three steps. First we fit a triaxial ellipsoid model to the data to get the overall extents of the object. We then moved on to an 8th-degree-and-order spherical harmonics model to fit for the global-scale topography seen in the images. Finally, in order to fit for the small-scale features, we used a vertex model with 1000 vertices and 1996 triangular facets. This choice yields a facet resolution of ∼50 m, which is comparable to the best range resolution. In each step, weighted penalty functions were used to favor models with uniform density, principal axis rotation, and a reasonably smooth surface. We used a cosine law to model the radar scattering from the surface of the asteroid:

$$\frac{d\sigma}{dA} = R(C+1)(\cos\alpha)^{2C}. \quad (1)$$

Here, σ is the radar cross section, A is the target surface area, R is the Fresnel reflectivity, C is a parameter related to the near-surface roughness of the asteroid at the radar wavelength scales, and α is the incidence angle of the wave. Values of C close to 1 represent diffuse scattering, whereas larger values represent more specular scattering (Mitchell et al. 1996).

Because nonlinear least-squares methods tend to find local minima when searching a wide parameter space, we carried out an extensive grid search for the best-fit spin axis orientation during the ellipsoid and spherical harmonics shape modeling stages. We assumed that the light curve period of 2.775 hr (Pravec et al. 2006) provided a good approximation to the sidereal spin period and we fit shape models to the data using spin axis orientations in increments of 15° in ecliptic longitude (λ) and 15° in ecliptic latitude (β). For each case, we performed an ellipsoid model fit followed by an 8th degree spherical harmonics model fit. Only the following shape parameters were allowed to change: the semi-axes in the ellipsoid fit and spherical harmonic coefficients in the spherical harmonic fit, the initial rotational phase of the object, and the radar scattering parameter R. The spin rate, the spin axis orientation, and the radar scattering parameter C were kept fixed. The grid search was repeated for $C = 0.6$, 0.8, 1.0, and 1.2. We defined a somewhat arbitrary threshold separating acceptable fits from poorer solutions by visually comparing the synthetic and observed images and using a χ^2_ν threshold of 0.665.

Our mutual orbit pole estimates lie in the region where spin axis orientations were considered acceptable on the basis of the shape model fits. Because we did not obtain a tight constraint on our spin pole using the shape model search (Section 3.2), we used the best-fit mutual orbit pole as the preferred spin pole for shape modeling. For a binary formed by a spin-up process, one would expect the primary spin pole to be roughly aligned with the mutual orbit pole, and tidal processes are expected to damp any residual inclination. With this spin pole assumption we fit 8th-degree-and-order spherical harmonics models to the data in the same way as we did in the grid search. Here we tried values of sidereal spin rate ranging from 3111° day^{-1} ($P = 2.777$ h) to 3117° day^{-1} ($P = 2.772$ hr) in steps of 0.2° day^{-1} and values of C ranging from 0.5 to 1.5 in steps of 0.1. As explained in Section 2.2, the shape modeling was done iteratively with the mutual orbit fits: mutual orbit fits were followed by shape model fits. In the second/final iteration, we performed the spherical harmonics shape model fit followed by a vertex model fit. At each step, we verified the quality of the fit by visually comparing the synthetic data generated by `shape` with the corresponding observed data. For the vertex model fit we used as initial conditions the best-fit spin state and spherical harmonics shape model determined at the previous step. Once again, only the shape parameters (location of the vertices), the initial rotational phase, and the radar scattering parameter R were allowed to change, and all the other parameters were kept fixed.

2.4. Secondary Shape and Spin State

Shape modeling of the secondary component was performed using a method similar to the one described in Section 2.3. The data set for modeling the shape and rotation of the secondary consisted of 180 Arecibo images taken between 2008 September 10 and 15. We left out images with 75 m range resolution from September 18 and 21 because the secondary was barely resolved in these images, and because these images did not improve the quality of the shape model fits. This time it was the primary that was edited out of the images. The CW spectra were not used because we were not able to completely remove the contribution of the primary from the total echo power. We fit an ovoid shape model,[8] followed by a 5th-degree-and-order spherical harmonic model. We then fit a vertex model with 150 vertices and 296 facets.

Table 2
Mutual Orbit Parameters for 2000 DP107

Parameter	Value from Margot et al. (2002)	Value From this Work
Semi-major axis (km)	2.62 ± 0.16	2.659 ± 0.08
Period (days)	1.755 ± 0.007	1.7556 ± 0.0015
Eccentricity	0.01 ± 0.01	0.019 ± 0.01
System mass ($\times 10^{11}$ kg)	4.6 ± 0.5	4.834 ± 0.45
Orbit pole (λ, β) (°)	(283, 67) ± 10	(294, 78) ± 10
Reduced χ^2	0.32	0.23

Periodicities detected in photometric data suggest that the secondary spin period may be close to 1.76 days (Pravec et al. 2006). This can be used as a guide in our shape modeling process, being mindful that light curve periods are neither sidereal nor synodic, whereas the `shape` software uses sidereal spin periods. This periodicity is close to the 1.7556 day orbital period (Table 2), confirming the finding that the secondary is locked in a 1:1 spin–orbit resonance (Margot et al. 2002). We used the radar-derived sidereal orbital period as the nominal spin period of the secondary for the purpose of shape modeling.

As with the primary, a grid search did not lead to a conclusive result about the spin axis orientation. Absent recent perturbations, one expects the spin pole of a tidally evolved secondary to be closely aligned with the mutual orbit pole, and we used the mutual orbit pole as the spin pole of the secondary. This proximity to the orbit pole can be verified by computing the obliquity of Cassini state 1 (Peale 1969), which is the state toward which tides drive the satellite spin pole. The other Cassini states are either unstable or the spin of the satellite is unstable at those Cassini states (Gladman et al. 1996). The obliquity can be computed using the following equation derived from Gladman et al. (1996) for a synchronous secondary:

$$\frac{3}{2}\left(\frac{C-\frac{A+B}{2}}{C}\right)\left[\frac{\sin\theta\cos\theta}{\sin(\theta\pm i)}\right]=\left(\frac{\dot{\Omega}}{\omega}\right). \quad (2)$$

Here $A < B < C$ are the the principal moments of inertia of the secondary, θ is the obliquity of the secondary spin pole with respect to the mutual orbit pole, i is the inclination of the mutual orbit with respect to the invariable plane (in this case it is approximately the equatorial plane of the primary), $\dot{\Omega}$ is the precession rate of the mutual orbit, and ω is the spin rate of the secondary. After the mutual orbit and the primary and the secondary shapes were fit (Sections 3.1, 3.2, and 3.3), we evaluated Equation (2) with the relevant values and found that $\theta < 1°$, confirming that the expected obliquity is small.

The initial rotation phase was set to a value such that the secondary was oriented with its minimum moment of inertia principal axis pointing toward the primary at pericenter. This is the expected configuration of a tidally locked satellite. The same radar scattering law as the one used for the primary was

[8] An ovoid is a distorted triaxial ellipsoid such that it has a wide and a narrow end.

used. We allowed the shape parameters and the radar scattering parameter R to change. The spin rate, the spin axis orientation, and the radar scattering parameter C were kept fixed. During the ovoid model stage, we attempted shape model fits with values of spin period ranging from 1.6 to 1.9 days in steps of 0.01 days.

An elongated and synchronous secondary in an eccentric orbit about the primary exhibits librations, which are oscillations about uniform rotation (e.g., Murray & Dermott 1999). A tidally evolved satellite is expected to exhibit a relaxed-mode libration (Naidu & Margot 2015), which is equivalent to a forced libration (Murray & Dermott 1999) when the spin–orbit coupling is negligible. This libration is roughly sinusoidal for small eccentricities and its amplitude as a function of the satellite elongation was estimated by Naidu & Margot (2015) using numerical simulations.

Because the mutual orbit is eccentric ($e \simeq 0.02$) and the secondary is elongated (Sections 3.1 and 3.3), we allowed for the possibility of relaxed-mode libration in longitude in the rotational model. For small amplitudes of forced librations and small orbital eccentricities, the deviation of the secondary orientation from regular circular motion ($\delta\phi$) can be approximated as

$$\delta\phi \approx A_{\rm lib} \sin\left[\omega_{\rm f}(t - t_0) + \pi\right], \quad (3)$$

where $A_{\rm lib}$ is the amplitude of the forced librations, $\omega_{\rm f}$ is the forcing frequency, which is equal to the mean orbital motion ($n = 2\pi/P$), and t_0 is the time of pericenter passage. The additional phase of π appears because for a synchronous secondary whose natural libration frequency is smaller than the forcing frequency, the librational phase is expected to be 180° at pericenter (Murray & Dermott 1999). We repeated the ovoid and spherical harmonics shape model fits with libration amplitudes ranging from 0° to 10° in steps of 1°. We tried all possible libration phases in steps of 4° in order to cover the libration phase uncertainty that arises due to an almost circular orbit. The libration amplitudes and phases were held at fixed values in each of these fits.

Results of the secondary shape and spin state modeling are discussed in Section 3.3.

2.5. Radar Scattering Properties

We transmitted circularly polarized waves and used two separate channels to receive echoes with the same circular (SC) and opposite circular (OC) polarization as that of the transmitted wave (Ostro 1993). We summed consecutive Arecibo CW runs from 2008 (Table 1) and measured the power received in the OC and SC channels. The ratio of the power received in SC to the power received in OC yields the circular polarization ratio, which is often denoted by μ_C. We also used Equation (1) of Ostro (1993) to compute the radar cross-section of the target, which has the dimensions of surface area. We computed the dimensionless *specific radar cross-section* ($\hat{\sigma}$), also called the *radar albedo*, with the OC CW spectra by taking the ratio of the radar cross-section to the geometric cross-sectional area of the target (primary + secondary) at the time of the observations. We used `shape` to compute the orientations of the target and corresponding projected areas at the times of CW runs.

The procedure described in the previous paragraph yielded values of $\hat{\sigma}$ and μ_C that combine the echoes from both the primary and secondary. We were also interested in estimates of these quantities for the secondary component alone. We obtained these by removing the contribution of the primary from the OC CW spectra. This subtraction was performed by fitting a 5th degree polynomial to the primary CW spectra and by masking out the frequency bins that contained a contribution from the secondary. After subtraction, we estimated $\hat{\sigma}$ and μ_c for the secondary using the same procedure as that described in the previous paragraph. Results are given in Section 3.4.

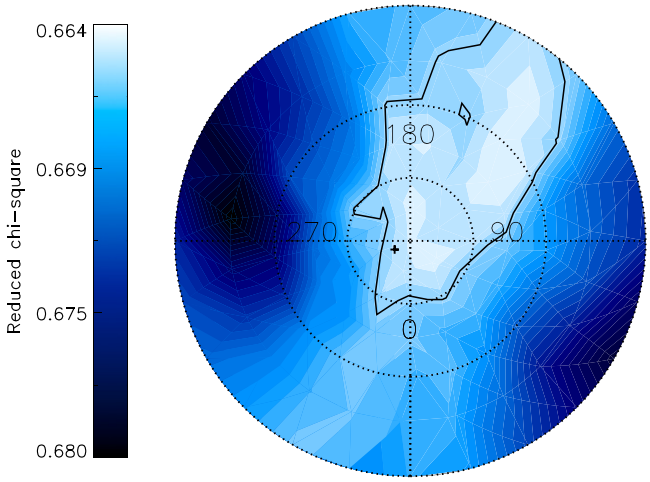

Figure 1. Contour plot of the goodness of fit (χ^2_ν) of shape models with different spin axis orientations on a polar stereographic projection of the celestial sphere, looking down the ecliptic north pole. Numbers indicate ecliptic longitudes (λ). Dotted circles (outside to inside) show latitudes 0°, 30°, and 60°. The region enclosed by a solid black contour line ($\chi^2_\nu = 0.665$) shows acceptable shape model fits. The plus sign shows our mutual orbit pole estimate.

2.6. Mass Ratio, Component Masses, and Densities

The COMs of the two components follow roughly Keplerian orbits around the system COM, while the system COM or barycenter orbits the Sun. The motion of the primary COM relative to the system COM is called the reflex motion of the primary. We estimated the mass ratio of the components and the reflex motion of the primary by quantifying the goodness of fit of heliocentric orbit fits using the astrometry of the system COM under various mass ratio assumptions.

The system COM lies on the line joining the component COMs at a distance of $d_{\rm p}$ from the primary and a distance of $d_{\rm s}$ from the secondary. The ratio of these distances ($d_{\rm s}/d_{\rm p}$) is equal to the primary-to-secondary mass ratio ($M_{\rm p}/M_{\rm s}$). For a given mass ratio assumption, we calculated the ratio $d_{\rm s}/d_{\rm p}$ and estimated the barycenter locations along the lines joining the component COMs in each of the 278 images obtained in 2008 that were used for shape modeling. This provided estimates of the two-way ranges of the system COM, where we once again used the `shape`-based component COMs determined to sub-pixel accuracy. We explored mass ratio assumptions from $M_{\rm p}/M_{\rm s} = 15$ to 30 in steps of 0.1 to determine the corresponding two-way ranges of the system COM and assigned uncertainties equal to the range resolution. For each mass ratio assumption we then performed a fit for the heliocentric orbit to all available optical astrometry and the system COM ranges. The best overall fit, as indicated by the

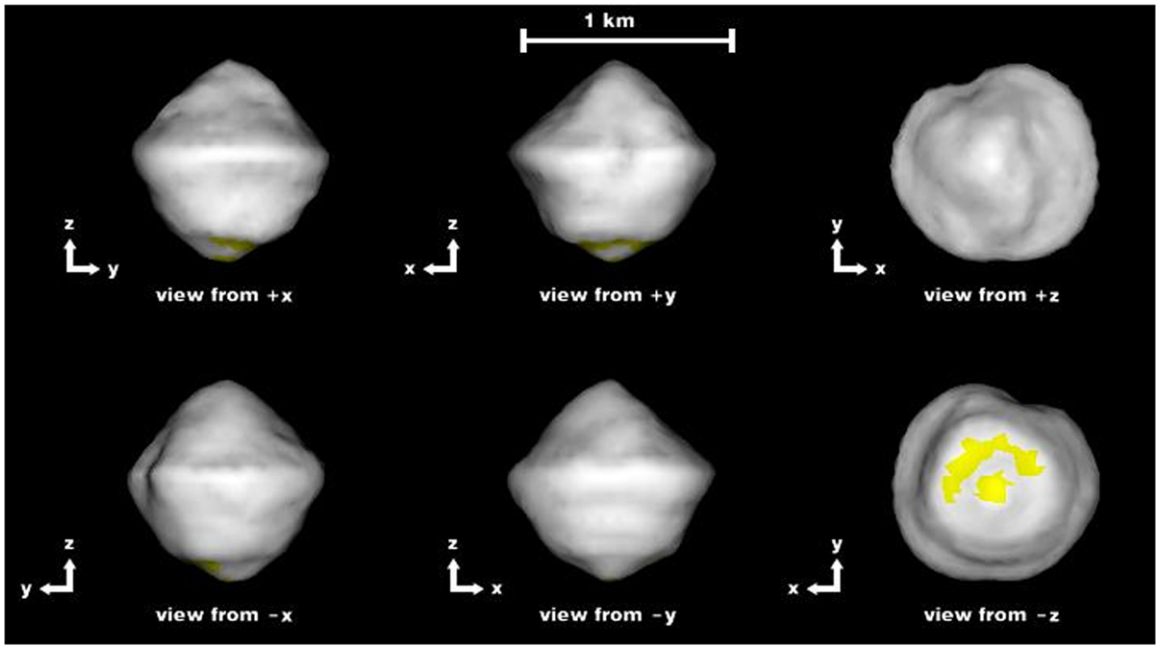

Figure 2. Vertex shape model of the primary as seen along the three principal axes *x, y,* and *z*. For principal axis rotation, the spin axis is aligned with the *z* axis. Yellow regions have radar incidence angles >60° and hence are not well constrained. The shape model has 1000 vertices and 1996 triangular facets. The effective surface resolution is ∼57 m.

lowest sum of squares of the residuals, yielded an estimate of the actual mass ratio of the system.

We used the mass ratio to apportion the total mass of the system, estimated from the mutual orbit, to the primary and the secondary. These mass estimates were divided by the corresponding component volume estimates, obtained from shape models, to yield component density estimates.

2.7. Primary Gravitational Environment

We used the primary shape model and density estimate to compute the gravity field on the surface of the primary, under a uniform density assumption. The acceleration on the surface is the vector sum of the gravitational acceleration due to the primary's mass and the centrifugal acceleration due to its spin. An acceleration vector was computed at the center of each facet using the method described in Werner & Scheeres (1997). The gravitational slope, which is the angle that the acceleration vector makes with the local inward-pointing surface-normal vector, was also computed for each facet.

3. RESULTS

3.1. Mutual Orbit

Our shape modeling results showed that the oblateness J_2 of the primary is about 0.03 (Section 3.2), such that the difference between observed and osculating orbital elements (Greenberg 1981) is small. Specifically, the quantity $\frac{3}{2}J_2(R_p/a)^2$ (R_p is the primary radius and a is the semimajor axis), which represents the fractional difference between the observed and osculating values of the semimajor axis (Greenberg 1981), amounts to $\sim 10^{-3}$. If the orbital eccentricity exceeds this value, one can expect an orbital regime where the true and mean anomalies circulate while the longitude of pericenter precesses. For smaller values of the eccentricity, another class of orbit is possible, where the true and mean anomalies librate around pericenter while the longitude of pericenter circulates. For our purposes, both orbit types are well accommodated by fitting the observations to a Keplerian ellipse. However, the orientation of the ellipse may be different for the 2000 and 2008 observations. For reasons explained in Section 4.2, it was not possible to reliably fit for the apsidal precession rate.

The mutual orbit has a semimajor axis $a = 2.659 \pm 0.08$ km and a sidereal orbital period $P = 1.7556 \pm 0.0015$ days. *Kepler*'s third law yields $GM_T = 32.24 \pm 3.00\ m^3\ s^{-2}$, where G is the gravitational constant and M_T is the total mass of the system. Substituting $G = 6.67 \times 10^{-11}\ m^3\ kg^{-1}\ s^{-2}$, we find $M_T = 4.834 \pm 0.45 \times 10^{11}$ kg. Table 2 lists the best-fit orbital parameters obtained using the combined 2000 and 2008 data and compares it to the values published in Margot et al. (2002). The values from both works are consistent with each other.

3.2. Primary Shape and Spin State

The result of our grid search for the best-fit spin pole is illustrated in Figure 1, which shows a contour plot of the χ_ν^2 values of the shape model fits for various orientations of the spin pole. Figure 1 shows the result for $C = 0.8$, which gave lower overall χ_ν^2 values than the other values of C that we tried. However, the general χ_ν^2 patterns are similar, irrespective of the value of C.

As explained in Section 2.3, we assumed the spin pole to be aligned with the mutual orbit pole at $\lambda = 294°$ and $\beta = 78°$. The best-fit sidereal spin period is 2.7745 ± 0.0007 hr. Radar scattering $C = 1.0$ yielded the shape model with the lowest χ_ν^2. Figure 2 shows the vertex shape model produced under these assumptions for the spin pole and the value of C, Table 3 lists the associated parameters, and Figure 3 shows examples of the observed images and the fits using this model. The model shows a good general agreement with the data.

An equatorial ridge similar to the one found on the 1999 KW4 primary (Ostro et al. 2006) is clearly seen. However, the

Table 3
Primary and Secondary Shape Model Parameters

Parameters		Primary	Secondary
Extents along	x	0.992 ± 5%	0.379 ± 6%
Principal axes (km)	y	0.938 ± 5%	0.334 ± 6%
	z	0.964 ± 5%	0.270 ± 6%
Surface area (km^2)		2.481 ± 10%	0.329 ± 12%
Volume (km^3)		0.337 ± 15%	0.017 ± 18%
Moment of inertia ratios	A/C	0.914 ± 10%	0.708 ± 10%
	B/C	0.946 ± 10%	0.888 ± 10%
Equivalent diameter (km)		0.863 ± 5%	0.316 ± 6%
DEEVE extents (km)	x	0.899 ± 5%	0.377 ± 6%
	y	0.871 ± 5%	0.314 ± 6%
	z	0.821 ± 5%	0.268 ± 6%
Spin pole (λ, β) ($^\circ$)		(294, 78)	(294, 78)

Note. The shape model of the primary consists of 1000 vertices and 1996 triangular facets, corresponding to an effective surface resolution of ~57 m. The shape model of the secondary consists of 150 vertices and 296 facets; it has an effective surface resolution of ~52 m. Surface area is the surface area of the shape model measured at the model facet scale. The moment of inertia ratios were calculated assuming homogeneous density. A, B, and C are the principal moments of inertia, such that $A < B < C$. Equivalent diameter is the diameter of a sphere with the same volume as that of the shape model. A dynamically equivalent equal volume ellipsoid (DEEVE) is an ellipsoid with uniform density with the same volume and moment of inertia ratios as the shape model. The spin poles are assumed to be aligned with the mutual orbit pole.

ridge is not so regular and has a ~300 m concavity on one side, similar to (341843) 2008 EV5 (Busch et al. 2011). An equatorial ridge is necessary to fit the observed power profile behind the LE in the radar images. The expected power profiles from models with and without equatorial ridges are compared in Busch et al. (2011). The shape model shows another ridge-like structure forming a ring around the south pole.

3.3. Secondary Shape and Spin State

We found that including longitudinal libration in the secondary spin model did not improve the shape model fits significantly, so we adopted the shape model fit with no libration as the nominal shape model. The non-detection of libration could either be because the libration amplitude, which is predicted to be ~15 m by Naidu & Margot (2015), is less than the resolution of the images or the temporal and longitudinal coverage of the secondary is insufficient.

The best-fit sidereal spin period of the secondary is 1.77 ± 0.02 days. This is consistent with the radar-derived mutual orbit period suggesting that the secondary is spinning synchronously. Figure 5 shows the best-fit secondary vertex shape model fit using this period, Table 3 lists the shape model parameters, and Figure 4 shows some examples of the observed images and the fits using this model. There is good agreement between the model and the data. The secondary has a triangular pole-on silhouette with dynamically equivalent equal volume ellipsoid dimensions of 377 × 314 × 268 m.

3.4. Radar Scattering Properties

Measurements of the OC radar albedo and circular polarization ratio for the combined primary and secondary spectra using the Arecibo data obtained in 2008 are listed in Table 4. Their mean values are 0.179 ± 0.02 and 0.265 ± 0.03, respectively, where the uncertainties are the standard deviations

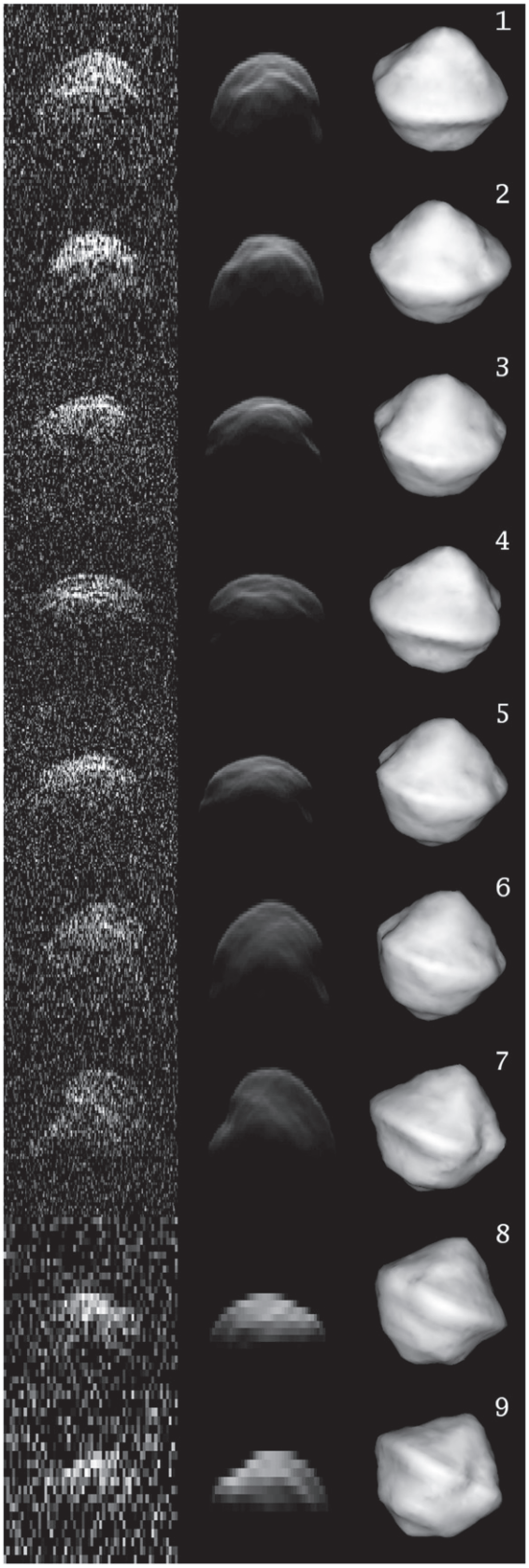

Figure 3. Examples of images and fits for the primary. Each row (from left to right) shows the observed image (single run), the corresponding synthetic image generated using the shape model, and the corresponding plane of sky view of the shape model. The images were obtained on (from top to bottom) September 10.43641, 10.47739, 11.41307, 11.46787, 13.37204, 15.33765, 15.38140, 18.30239, and 21.26607.

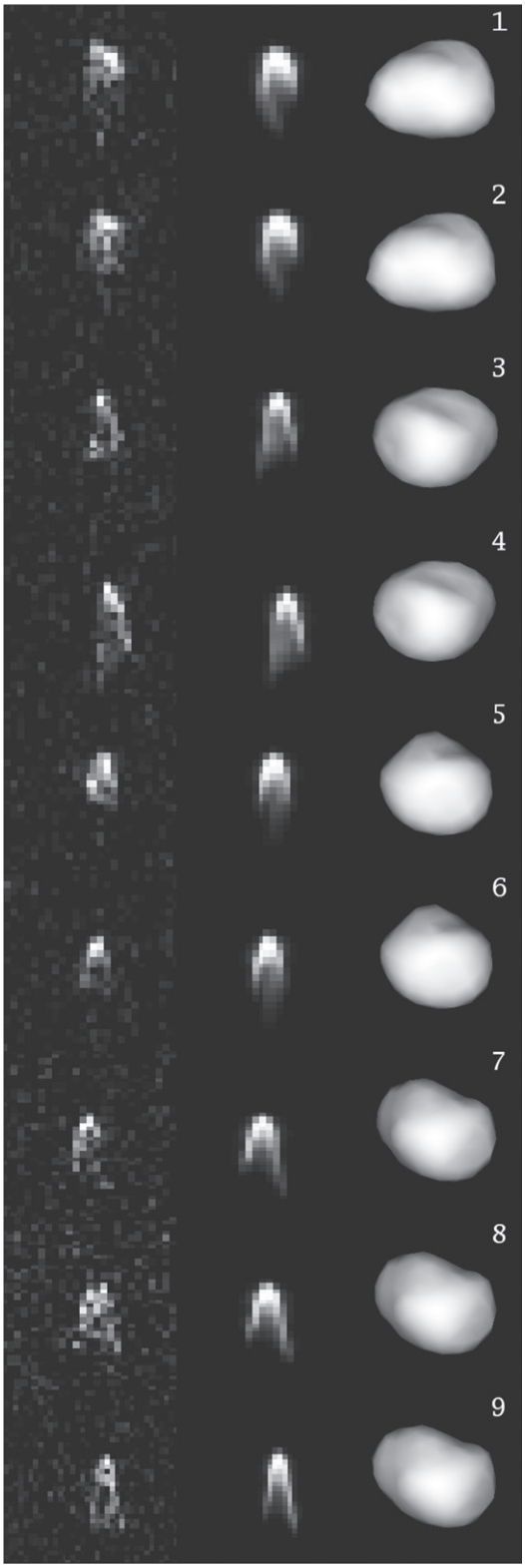

Figure 4. Examples of images and fits for the secondary. Each row (from left to right) shows the observed image (single run), the corresponding synthetic image generated using the shape model, and the corresponding plane of sky view of the shape model. The images were obtained on (from top to bottom) September 10.47192, 10.48012, 11.41307, 11.44529, 13.43063, 13.43896, 15.33765, 15.36390, and 15.39306.

of the individual measurements. The mean value of the circular polarization ratio is close to the median value (0.26) for all NEAs and is most consistent with the S- and C-class asteroids (Benner et al. 2008). Figure 6 shows Arecibo OC and SC CW spectra obtained on 2008 September 11.

The last two columns of Table 4 show the OC radar albedos and circular polarization ratios for the power spectra containing only the estimated secondary contribution. Their mean values are 0.174 ± 0.05 and 0.326 ± 0.08, respectively. The radar albedo of the secondary alone is equivalent to that of the primary+secondary, suggesting that both components have identical composition. The polarization ratio of the secondary appears to be more variable and greater than that of the primary, suggesting that the secondary may be rougher than the primary at radar wavelength scales. However, the difference is within the 1 standard deviation of the measurements, preventing a more definite conclusion.

3.5. Mass Ratio, Component Masses, and Densities

Direct estimation of the mass ratio using the method described in Section 2.6 yielded a mass ratio (M_p/M_s) of 26.2 ± 2. This mass ratio corresponds to a reflex motion of the primary of 98 ± 8 m, consistent with the estimate of 140 ± 40 m of Margot et al. (2002) and with the apparent motion observed directly in the images. Figure 7 shows a plot of the χ^2 values of the heliocentric orbit fits to the optical and radar astrometry. The latter uses two-way ranges to the system COM as determined under various mass ratio assumptions as discussed in Section 2.6. Using this mass ratio we can apportion the total mass of the system (M_T) to the two components. We find the mass of the primary and the secondary to be 4.656 ± 0.43 × 10^{11} kg and 0.178 ± 0.021× 10^{11} kg, respectively. Dividing the masses by the volumes of the corresponding shape models, we find densities for the primary and secondary to be 1381 ± 244 and 1047 ± 230 kg m^{-3}, respectively, where the largest source of uncertainty comes from the volume determinations. The densities are similar, pointing toward a similar composition and porosity.

3.6. Primary Gravitational Environment

The acceleration map on the surface of the primary shape model shows that, for nominal values of mass, spin period, and shape parameters, the net acceleration on the equatorial ridge is very close to zero (Figure 8), which implies that the centrifugal acceleration on the ridge almost cancels out the acceleration due to the primary's mass. As we move to higher latitudes, and hence closer to the spin axis, the magnitude of the centrifugal acceleration decreases, causing the magnitude of the net acceleration to increase and reach values up to 159 μm s^{-2} at the poles. This value is about 1.6 × 10^{-5} times that on Earth.

The gravitational slopes near the poles are close to zero (Figure 9). Around the mid-latitudes, the slopes are higher and most regions here have values between 40° and 65°. Regions on the equatorial ridge have slopes close to 180°, implying that the magnitude of centrifugal acceleration is greater than the magnitude of acceleration due to mass. Inside the concavity on the equatorial ridge the slopes are close to 0°. These slopes provide clues to the mechanical properties of the asteroid material. The implications are discussed in Section 4.

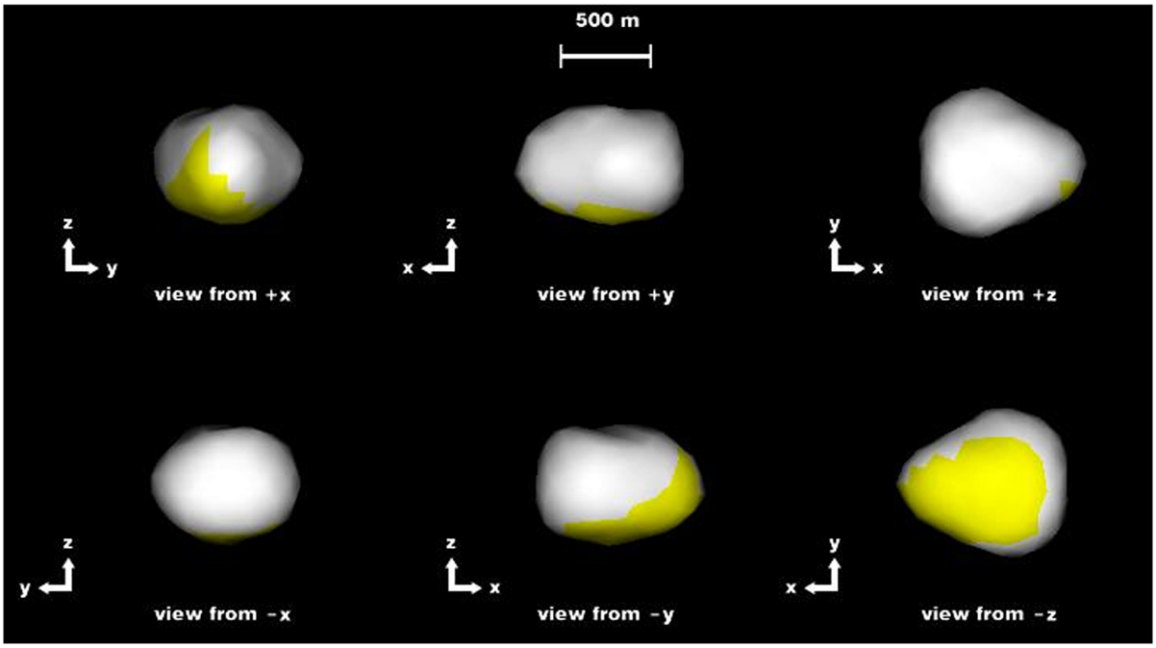

Figure 5. Secondary shape model as seen along the three principal axes. The top right view is along the positive spin axis. The positive x axis points toward the primary. Yellow regions have radar incidence angles $>60^\circ$ and hence are not well constrained. The shape model has 150 vertices and 296 triangular facets. The effective surface resolution is ~52 m.

Table 4
Radar Scattering Properties

UT Date	Set	Prim.+Sec.		Secondary	
yyyy-mmm-dd		$\hat{\sigma}_{OC}$	μ_C	$\hat{\sigma}_{OC}$	μ_C
2008 Sep 10	1	0.158	0.334	0.245	0.334
2008 Sep 10	2	0.239	0.248	0.154	0.238
2008 Sep 11	1	0.186	0.261	0.098	0.413
2008 Sep 11	2	0.186	0.258	0.136	0.316
2008 Sep 13	1	0.197	0.275	0.159	0.458
2008 Sep 13	2	0.187	0.236	0.226	0.265
2008 Sep 15	1	0.184	0.241	0.205	0.218
2008 Sep 15	2	0.159	0.294	0.149	0.373
2008 Sep 18	1	0.158	0.247	0.125	0.443
2008 Sep 18	2	0.160	0.242	0.149	0.283
2008 Sep 21	1	0.180	0.234	0.229	0.254
2008 Sep 24	1	0.163	0.292	0.176	0.338
2008 Sep 24	2	0.157	0.276	0.211	0.299
Average		0.179	0.265	0.174	0.326
St. dev.		0.02	0.03	0.05	0.08

Note. Radar albedos $\hat{\sigma}_{OC}$ and circular polarization ratios μ_C of the primary and secondary combined (columns 3 and 4) and of the secondary alone (columns 5 and 6) measured on the basis of Arecibo data (Table 1). Except for September 21, two measurements were available per day (distinguished by the index in the second column).

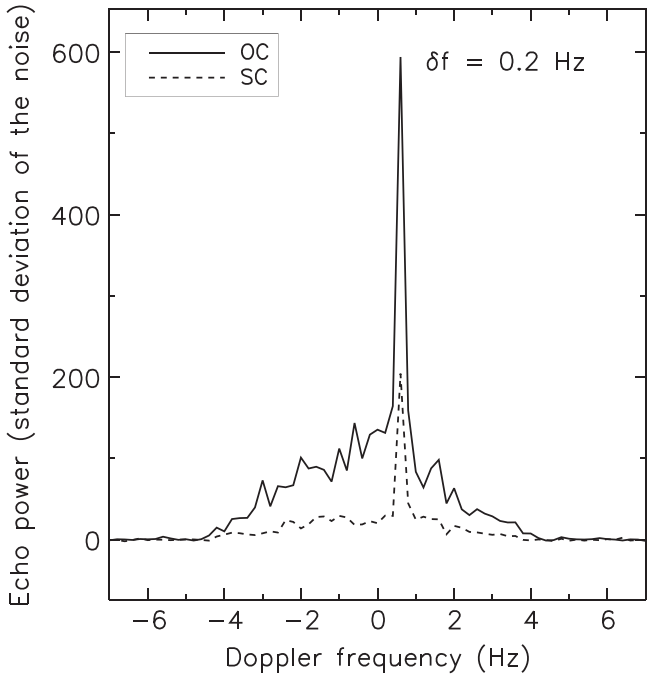

Figure 6. Representative OC and SC CW spectra obtained at Arecibo on UT 2008 September 11.483. The broad component is due to the primary with a 2.77 hr spin period. The narrow spike is due to the secondary with a 1.77 day spin period.

4. DISCUSSION

4.1. Primary Shape and Gravitational Environment

The primary shape is similar to shapes of some other radar-characterized asteroids such as (66391) 1999 KW4, (136617) 1994 CC, (341843) 2008 EV5, (101955) Bennu, etc. (Ostro et al. 2006; Brozović et al. 2011; Busch et al. 2011; Nolan et al. 2013, respectively). This commonly observed top-shaped structure is an indication that the asteroid has undergone reshaping, most likely due to the spin-up of the primary (e.g., Harris et al. 2009). The shape and the gravitational field provide clues about the mechanical properties of the material of the primary. Figure 9 shows that the gravitational slopes around the mid-latitudes are mostly between 40° and 65°. Some of these values are greater than the angle of repose of sand on Earth, which has values between 30° and 50°. A possible

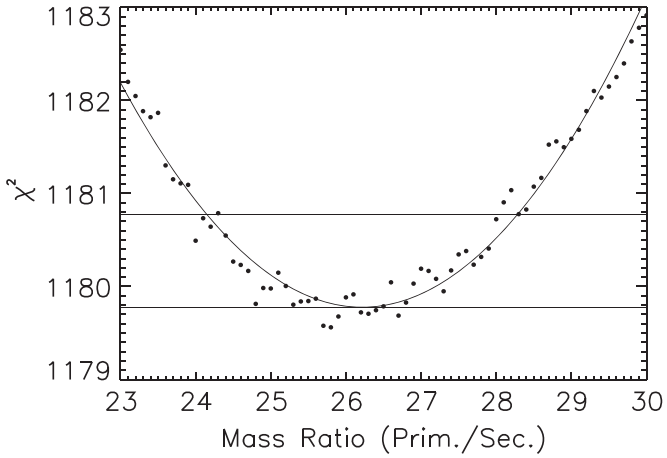

Figure 7. Points show χ^2 values of heliocentric orbit fits to optical and radar astrometric observations. Radar astrometry includes two-way ranges of the system COM under various mass ratio assumptions. Solid curve shows the best-fit parabola to the χ^2's. The horizontal lines show the minimum χ^2 on the parabola and the χ^2 corresponding to the 1σ uncertainty, respectively. The minimum χ^2 corresponds to a primary-to-secondary mass ratio of 26.2 ± 2.

explanation for such high angles is that cohesive van der Waals forces between the particles play an important role on the surfaces of the asteroids, as proposed by Scheeres et al. (2010). These cohesive forces could be comparable in magnitude to the ambient gravitational force (Scheeres et al. 2010), resulting in much higher effective angles of repose (>50°) than the material can sustain (e.g., Rognon et al. 2008). Figure 9 shows that slopes at the equator of the primary are >90°, implying that centrifugal force is greater than the gravitational pull at the equator. In the absence of other forces, this imbalance will cause material to escape from the primary at the equator. Cohesion between particles could balance the excess centrifugal force and prevent such an escape. Nevertheless, the regions in the mid-latitudes with high slopes might be devoid of fine grained material, as the material would slide off to lower potential areas. Some of the regions on the equatorial ridge with slopes close to 180° might also be paths through which material is shed off from the primary. The slope values are sensitive to the size, the density, and the spin period of the asteroid. Scaling down the asteroid by ∼5% and keeping the mass unchanged (effectively increasing its density by ∼16%, which is within the density uncertainty) yields slopes close to zero on most regions at the equator and slopes lower than 45° on most of the surface of the asteroid. If tides and/or YORP spin down the asteroid, there will be a global decrease in the

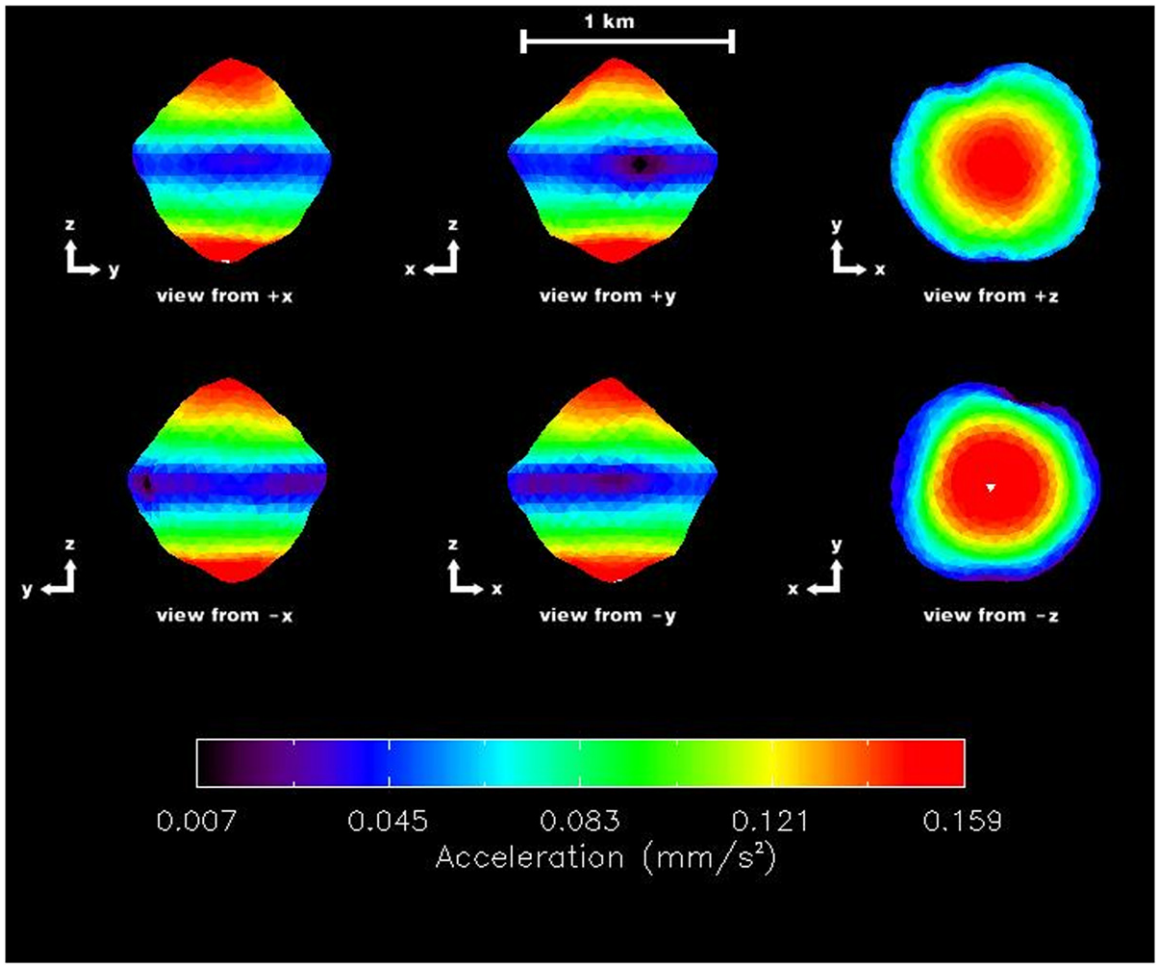

Figure 8. Magnitudes of the vector sum of acceleration due to gravity and centrifugal acceleration computed at the centers of the facets of the primary shape model. We assumed a uniform density of 1381 kg m^{-3}, which was obtained in Section 3.5, and a spin period of 2.7745 hr. At the equator the values are close to zero, indicating that the magnitude of centrifugal acceleration is almost equal to the magnitude of acceleration due to the asteroid's mass.

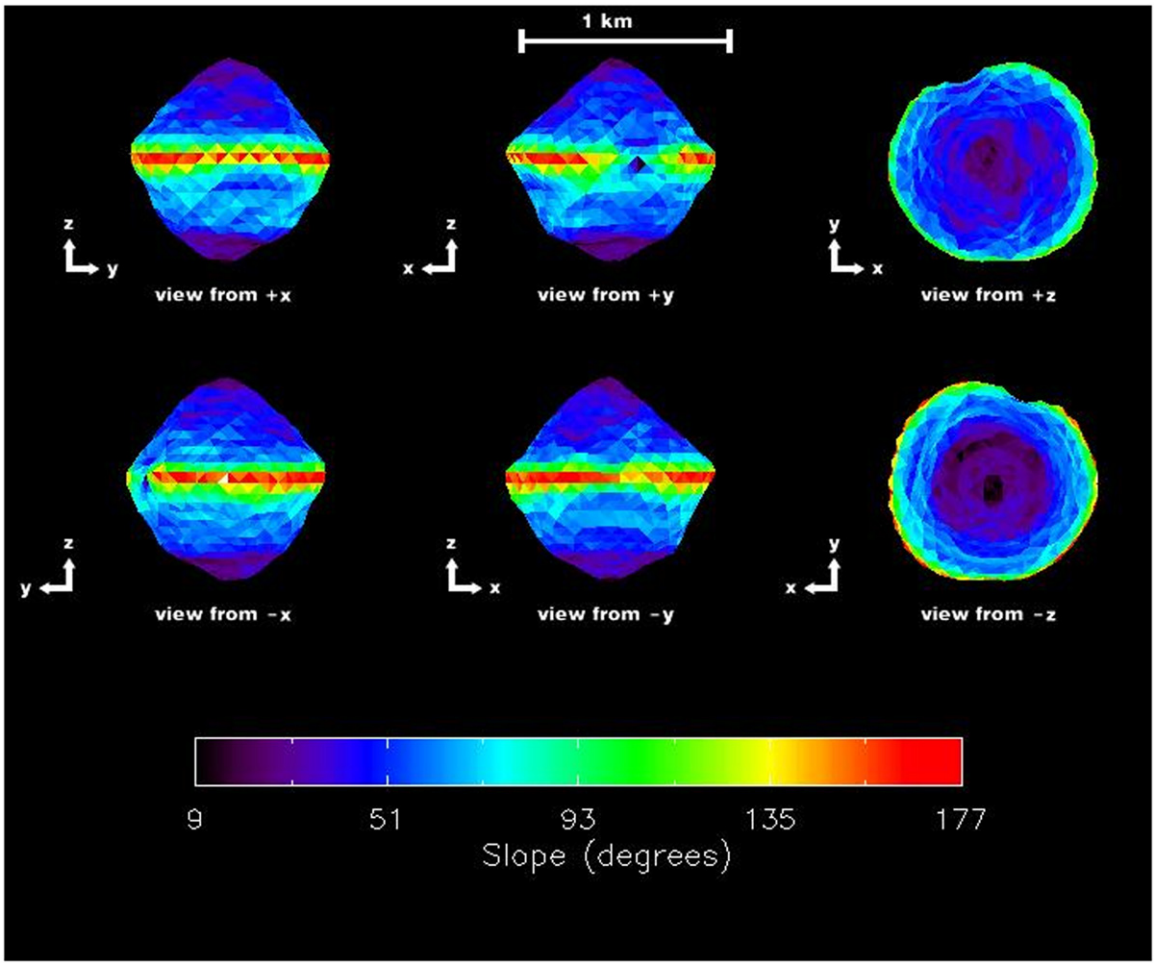

Figure 9. Gravitational slopes computed at the centers of the facets of the primary shape model. We assumed a uniform density of 1381 kg m^{-3}, obtained in Section 3.5, and a spin period of 2.7745 hr. Slopes vary from ∼0° at the poles and some regions at the equator to close to 180° at most regions at the equator. Most regions at mid-latitudes have slopes between 40° and 65°.

slopes. A similar spin down might have led to the overall low slopes seen on 2008 EV5 (Busch et al. 2011).

Assuming a grain density of 3000 kg m^{-3}, which would be appropriate for an S-type asteroid, the observed densities of the primary and secondary can be explained by ∼55% and ∼65% porosity, respectively. Dilation of cohesive materials during avalanching flows seen in numerical simulations and laboratory experiments (e.g., Alexander et al. 2006; Rognon et al. 2008) could also explain the high porosity needed to match the low densities of the primary and the secondary.

The equatorial ridge has an approximately 300 m concavity on it. The concavity could just be a void left over after the asteroid attained its current shape or it could be an impact crater. Jacobson & Scheeres (2011a) hypothesized that a secondary fission event could take place during the post-fission dynamics following the binary formation process, and that one of the fragments may impact the primary. Secondary fission refers to the rotational fission of the secondary as it is torqued by spin–orbit coupling while in a chaotic rotation state (Jacobson & Scheeres 2011a; Naidu & Margot 2015). Gravitational pull dominates the centrifugal force in the interior of the concavity, so ponding of fine grained material transported from higher latitudes can be expected inside the crater.

4.2. Mutual Orbit

The eccentricity of the mutual orbit, $e \approx 0.019$, translates to a variation of the primary–secondary distance of $2ae \approx 100$ m during each orbit. While this variation is detectable in the radar data from 2008, which has a range resolution of 30 m, it is barely detectable in the radar data obtained in 2000, which has a range resolution of 75 m. Our determination of the longitude of pericenter therefore relies on the 2008 data only. Although we were not able to fit an orbital precession rate, our method does not rule out substantial pericenter precession during 2000–2008. We performed numerical simulations using the method developed by Naidu & Margot (2015) to estimate pericenter precession rates under various gravitational perturbations: the non-spherical mass distribution of the primary causes pericenter precession of about 90° year^{-1}, whereas the non-spherical mass distribution of the secondary contributes about −15° year^{-1}. The combined effect causes the pericenter to precess by about 75° year^{-1} in a prograde direction with respect to the mutual orbit. Additionally, the gravitational perturbations from the Sun cause the pericenter to precess by about 10° year^{-1}. The combined effect of these three gravitational perturbations is a secular apsidal precession rate of about 85° year^{-1}, but there are significant short-term variations in the

precession rate, making detection of apsidal precession difficult. Gravitational perturbations from planets and radiative forces from the Sun complicate the dynamics further.

The mutual orbit normal (and the assumed primary and secondary spin poles) is separated by about 5° from the heliocentric orbit normal, which is common among binary NEAs and possibly indicative of YORP obliquity evolution (Rubincam 2000).

4.3. Binary YORP

Binary YORP is a radiative torque that is hypothesized to alter the mutual orbit of synchronous binary systems (Ćuk & Burns 2005). A synchronous satellite has a fixed leading and trailing side with respect to the direction of its orbital motion, so an asymmetric re-radiation from the surface of the satellite will lead to a net torque on the mutual orbit. A potentially observable signature of such a torqued orbit is a quadratic change in the mean anomaly of the satellite (McMahon & Scheeres 2010). Detecting a quadratic change in mean anomaly requires measurements of the mean anomaly on a minimum of three widely separated epochs. Additional measurements will be required to model the complicated dynamics described in the previous section. 2000 DP107 is a prime candidate for the detection of binary YORP since it presents repeated opportunities for observations and has already been observed in 2000 and 2008 by radar and in 2000, 2008, 2011, and 2013 by optical telescopes. McMahon & Scheeres (2010) made a mean anomaly drift rate prediction for 2000 DP107 by scaling the results obtained from the radar-derived shape model of the satellite of 1999 KW4. Those predictions can now be updated using the secondary shape model. Depending on the direction of the binary YORP torque, the mutual orbit could either expand, contract, or remain unchanged. The outcomes of these scenarios were studied in detail by Jacobson & Scheeres (2011a). An expanding mutual orbit could lead to the formation of asteroid pairs or an asynchronous satellite, whereas a contracting mutual orbit could create a contact binary asteroid (e.g., Taylor & Margot 2011). A contracting binary YORP torque could also be balanced by an equal and opposite tidal torque, implying a binary asteroid in a stable equilibrium as hypothesized by Jacobson & Scheeres (2011b). Future observations of this system may provide a detection of binary YORP evolution.

4.4. Formation and Evolution

The normalized total angular momentum of a binary asteroid system (J/J') provides clues to the formation mechanism of the system. In this expression, J is the total angular momentum and $J' = \sqrt{GM_{\rm sys}R_{\rm eff}}$, where $M_{\rm sys}$ and $R_{\rm eff}$ are the total mass and equivalent radius of the binary system. Ratios greater than 0.4 in NEAs are consistent with formation of the binary by mass shedding due to spin-up of the parent body (Margot et al. 2002; Pravec & Harris 2007; Taylor & Margot 2011). 2000 DP107 has a separation $a/R_{\rm p} \simeq 6.2$ that is larger than most known binary NEAs and a low eccentricity of 0.019, resulting in $J/J' \sim 0.49$. This is much larger than is necessary for spin fission. In a tides-only model, this large separation implies a rather weak primary, an old age compared to the dynamical lifetime of NEAs, or the influence of another mechanism such as binary YORP and/or YORP for increasing the total angular momentum (Taylor & Margot 2011).

5. CONCLUSION

The radar observations of 2000 DP107 allowed us to produce shape models of the primary and secondary, estimate their masses and densities, compute the gravitational environment of the primary, and estimate the mutual orbit parameters. The shape model and gravitational environment of the primary provide important clues about the material properties of the asteroid. The shape model of the secondary can be used to estimate the evolution of the mutual orbit under the binary YORP torque. Future radar and photometric observations of the system may provide measurements of the evolution of the mutual orbit. The next radar and photometric observation opportunity is in 2016.

We thank Dan Scheeres and Seth Jacobson for useful discussions, and the anonymous reviewer for excellent suggestions. This material is based on work supported by the National Science Foundation under grant No. AST-1211581 and the National Aeronautics and Space Administration under grant No. NNX14AM95G.

REFERENCES

Alexander, A. W., Chaudhuri, B., Faqih, A. M., et al. 2006, Powder Technology, 164, 13
Benner, L. A. M., Nolan, M. C., Margot, J., et al. 2008, BAAS, 40, 432
Brozović, M., Benner, L. A. M., Taylor, P. A., et al. 2011, Icar, 216, 241
Busch, M. W., Ostro, S. J., & Benner, L. A. M. 2011, Icar, 212, 649
Ćuk, M., & Burns, J. A. 2005, Icar, 176, 418
Funase, R., Koizumi, H., Nakasuka, S., et al. 2014, in Small Satellite Conference 2014, 50 kg-Class Deep Space Exploration Technology Demonstration Micro-Spacecraft Procyon, 3
Gladman, B., Quinn, D. D., Nicholson, P., & Rand, R. 1996, Icar, 122, 166
Greenberg, R. 1981, AJ, 86, 912
Harris, A. W., Fahnestock, E. G., & Pravec, P. 2009, Icar, 199, 310
Hudson, S. 1993, Remote Sensing Reviews, 8, 195
Jacobson, S. A., & Scheeres, D. J. 2011a, Icar, 214, 161
Jacobson, S. A., & Scheeres, D. J. 2011b, ApJL, 736, L19
Magri, C., Ostro, S. J., Scheeres, D. J., et al. 2007, Icar, 186, 152
Margot, J. L., Nolan, M. C., Benner, L. A. M., et al. 2002, Sci, 296, 1445
Margot, J.-L., Pravec, P., Taylor, P., Carry, B., & Jacobson, S. 2015, arXiv:1504.00034
McMahon, J., & Scheeres, D. 2010, Icar, 209, 494
Mitchell, D. L., Ostro, S. J., Hudson, R. S., et al. 1996, Icar, 124, 113
Murray, C. D., & Dermott, S. F. 1999, Solar System Dynamics (Cambridge: Cambridge Univ. Press)
Naidu, S. P., & Margot, J.-L. 2015, AJ, 149, 80
Naidu, S. P., Margot, J.-L., Busch, M. W., et al. 2013, Icar, 226, 323
Nolan, M. C., Magri, C., Howell, E. S., et al. 2013, Icar, 226, 629
Ostro, S. J. 1993, RvMP, 65, 1235
Ostro, S. J., Margot, J. L., Benner, L. A. M., et al. 2006, Sci, 314, 1276
Peale, S. J. 1969, AJ, 74, 483
Pravec, P., & Harris, A. W. 2007, Icar, 190, 250
Pravec, P., Scheirich, P., Kušnirák, P., et al. 2006, Icar, 181, 63
Pravec, P., Wolf, M., & Šarounová, L. 1999, in IAU Coll. 173, Evolution and Source Regions of Asteroids and Comets, How many binaries are there among the near-Earth asteroids?, ed. J. Svoren, E. M. Pittich & H. Rickman (Tatranska Lomnica, Slovak Republic: Astronomical Institute of the Slovak Academy of Sciences), 159
Proakis, J. G., & Salehi, M. 2007, Digital Communications (New York: McGraw-Hill)
Rognon, P. G., Roux, J.-N., Naaïm, M., & Chevoir, F. 2008, JFM, 596, 21
Rubincam, D. P. 2000, Icar, 148, 2
Scheeres, D. J., Hartzell, C. M., Sánchez, P., & Swift, M. 2010, Icar, 210, 968
Taylor, P. A., & Margot, J.-L. 2011, Icar, 212, 661
Werner, R. A., & Scheeres, D. J. 1997, CeMDA, 65, 313